

Quantum valley Hall effect and perfect valley filter based on photonic analogs of transitional metal dichalcogenides

O. Bleu, D. D. Solnyshkov, and G. Malpuech

Institut Pascal, PHOTON-N2, University Clermont Auvergne, CNRS, 4 avenue Blaise Pascal, 63178 Aubière Cedex, France

(Received 13 March 2017; published 26 June 2017)

We consider theoretically staggered honeycomb lattices for photons which can be viewed as photonic analogs of transitional metal dichalcogenide (TMD) monolayers. We propose a simple realization of a photonic quantum valley Hall effect (QVHE) at the interface between two inverted lattices. This results in the formation of valley-polarized propagating modes whose existence relies on the difference between the valley Chern numbers, an analog of the \mathbb{Z}_2 topological invariant. We show that the magnitude of the photonic spin-orbit coupling based on the energy splitting between TE and TM photonic modes allows to control the number and propagation direction of these interface modes. Finally, we consider the interface between a staggered and a regular honeycomb lattice subject to a nonzero Zeeman field, therefore showing quantum anomalous Hall effect (QAHE). In such a case, the topologically protected one-way modes of the QAHE become valley-polarized and the system behaves as a perfect valley filter.

DOI: [10.1103/PhysRevB.95.235431](https://doi.org/10.1103/PhysRevB.95.235431)

I. INTRODUCTION

The band structure of a honeycomb lattice has been described in 1946 by Wallace within the tight-binding approximation [1]. The bands result from the coupling between the orbitals of the A and B atoms, and the Hamiltonian can be represented as an effective magnetic field acting on a pseudospin defined by the two sublattices (A and B). As widely advertised since the isolation of monolayer graphene, its dispersion contains two inequivalent Dirac points K and K' , located at the corners of the Brillouin zone. The effective field cancels at these points, where A and B orbitals are uncoupled. Around these points, the effective field is monopolar at K and Dresselhaus at K' : $H_{K,K'} = \hbar v_f(\tau_z q_x \sigma_x + q_y \sigma_y)$, where $\tau_z = \pm 1$ at K and K' , respectively, and $v_f = \frac{3aJ}{2\hbar}$ (a is the lattice parameter and J is the tunneling coefficient between the nearest neighbours). The two fields have opposite winding numbers (± 1 , respectively). A consequence is the π and $-\pi$ Berry phase acquired by an electron on a closed loop around the K and K' points, respectively [2].

In a staggered honeycomb lattice, A and B sites have an energy difference 2Δ [3]. In such a case, the effective field gains a Z component similar at both K and K' and the Hamiltonian becomes $H_{K,K'} = \hbar v_f(\tau_z q_x \sigma_x + q_y \sigma_y) + \Delta \sigma_z$. A gap opens between the bands, with the presence of a nonzero Berry curvature of opposite sign near K and K' . As a result, the total Chern number of the bands is zero and they are topologically trivial. This Hamiltonian is realized by several real crystalline structures, such as the TMD monolayers [4,5]. A large part of the unique properties of this class of 2D materials is due to the local Berry curvature of their bands near the K and K' points and to the related orbital moment. For instance, it imposes specific optical selection rules. Only circularly polarized σ^+ light can be absorbed by the K valley transition, while only σ^- light is absorbed by the K' valley transition [6,7]. The valley dependent Berry curvature is also at the origin of the valley Hall effect [4,8,9] recently observed experimentally in MoS₂ [10]. Electrons, accelerated by an electric field, experience a valley-dependent Berry

curvature provoking a valley-dependent drift perpendicular to the acceleration direction, which leads to spatial separation of valley electrons.

The valley degree of freedom allows to define a valley pseudospin. Moreover, the Berry curvature is typically strongly concentrated around K and K' , which allows to define a valley Chern number $C_{K,K'}$ [3] by analogy with the spin Chern number, which is linked to the \mathbb{Z}_2 topological invariant characterizing the quantum spin Hall effect (QSHE) [11]. One might think that similarly with the QSHE effect, the presence of this nonzero topological invariant should lead to the existence of surface states (at the edges of the sample) with valley dependent chirality. This is not the case, because the Bloch wave functions associated with the valleys are not the stationary eigenstates in the vacuum, contrary to the spin states, and are therefore mixed at such boundaries. In other words, the bulk-edge correspondence is not well defined for valley eigenstates since the two valleys do not exist in the vacuum. However, at an interface (domain wall) between two TMD analogs inverted the one with respect to the other, zero-line modes are known to be present [12]. These states can become valley-dependent and chiral with a proper choice of the lattice parameters [13] leading to the so-called quantum valley Hall effect (QVHE).

While it is possible to invert a real TMD lattice simply by turning the 2D sheet upside down, the interfaces between two inverted lattices cannot be formed, because they would correspond to metal-metal or chalcogenide-chalcogenide chemical bonds. It seems therefore very difficult to obtain and study chiral states at such interfaces. Several theoretical works have proposed to use bilayer graphene systems, where a tunable gap can be opened by applying a bias voltage [14,15] to organize these interface states [16–18]. Chiral valley-polarized edge states are also predicted in these systems due to the coupling between the two layers with a potential difference [19]. The signature of the existence of the interface modes has been reported experimentally in the bilayer system [20] and the study of valley polarized edge states or QVHE is nowadays a research field in several condensed matter systems [21–24].

TMD analogs can also be realized using cold atoms in optical lattices, or by coupling optical resonators. In the latter case, Berry curvature can be probed by resonant excitation of the Dirac point in momentum space and measurement of a drift of the wave packet, which, however, is predicted to be relatively small [25]. Recently, photonic quantum valley Hall effect in photonic crystal slabs [26–29] has been theoretically described. In these works, chiral valley polarized interface states are organized, but are not protected against disorder induced intervalley scattering.

In this work, we first propose to implement quantum valley Hall effect in a photonic system using a honeycomb lattice of coupled micropillars [30], with a tunable energy detuning between A and B pillars. The gap size can be entirely controlled by tuning the pillar diameter. In the second section, we consider the impact of the splitting between TE and TM optical modes, which is specific to photonic systems, which was not considered before. We show that the magnitude of the splitting allows to tune the direction of propagation and number of interface modes. In the last section, we propose an original scheme to build a perfect valley filter by using a domain wall between QAH and QVH phases using mixed light-matter exciton-polariton quasiparticles. The QAH phase for polaritons has been predicted to occur in different kind of polariton lattices under Zeeman field and is of current interest [31–34]. Obviously, the model used in this work is based on the honeycomb lattice. The dispersion of the interface modes as well as their real space propagation can be directly measured by optical spectroscopy techniques. The valley structure of a wave packet can be analyzed and controlled as well.

II. PHOTONIC QUANTUM VALLEY HALL EFFECT

An interesting aspect of using lattices of coupled photonic micropillars, like the one shown in Fig. 1(a), is that the tight-binding description is a very good approximation. The insertion of the quantum well in the optical cavity allows to achieve strong light matter coupling and to obtain exciton-polariton (polariton) eigenstates [35]. Thanks to their excitonic part, polaritons show a sizable Zeeman splitting between the two circular-polarized components under applied magnetic field in the growth direction or in the high density regime via spin-anisotropic interactions [36].

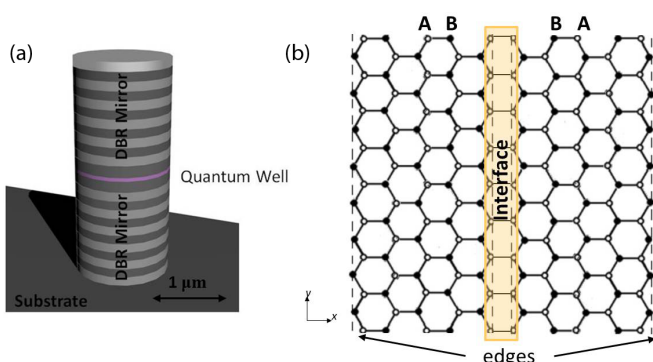


FIG. 1. (a) Cavity micropillar (artificial atom) scheme. (b) Zigzag interface between two TMD analog lattices with opposite A-B organization giving rise to zero lines modes and quantum valley Hall effect with a proper choice of parameters.

However, we will at first neglect the polarization degree of freedom. In this case, the tight-binding Hamiltonian describing the photonic states in the lattice of pillar cavities can be written as

$$H_k = \begin{pmatrix} \Delta_{AB} & -Jf_k \\ -Jf_k^* & -\Delta_{AB} \end{pmatrix}, \quad f_k = \sum_{j=1}^3 \exp(-i\mathbf{k}\mathbf{d}_{\phi_j}), \quad (1)$$

where $2\Delta_{AB}$ is the energy difference between the ground states of A and B pillars and J is the nearest neighbours tunneling coefficient. A nonzero Δ_{AB} leads to the opening of a band gap and induces opposite Berry curvatures around K and K' points, which for the “valence band” reads

$$B(q) = \tau_z \frac{9a^2 J^2 \Delta_{AB}}{(4\Delta_{AB}^2 + 9a^2 J^2 q^2)^{3/2}}. \quad (2)$$

Here, $\tau_z = \pm 1$ is the valley index. If Δ_{AB} is small, the Berry curvature is strongly localized around K points allowing to define the valley Chern numbers as $C_{K,K'} = \pm 0.5$. The total Chern number of the band $C = C_K + C_{K'}$ is zero. The flexibility of photonic systems allows to realize staggered graphene lattices with any sign of Δ_{AB} . The scheme proposed here is therefore to build an interface between two TMD analogs with opposite energy band gaps ($\Delta_{AB} < 0$ for $x < 0$ and $\Delta_{AB} > 0$ for $x > 0$) as first proposed theoretically in Ref. [12]. We stress that this kind of interface is not experimentally realistic for real electronic TMD monolayers. On the contrary, for the photonic analog that we propose and consider here, the gap sign is controlled by the sizes of the A and B micropillars. Such lattices and interfaces are very well within the current experimental possibilities [30,37].

We compute the dispersion of a ribbon with such interface (which can be considered as a domain wall) along the zigzag direction [see scheme Fig. 1(b)] using the tight-binding approach. The ribbon of size L is constructed with 128 coupled infinite zigzag chains, the interface is located in the middle of the ribbon. The dispersion of the full ribbon is plotted in Fig. 2(a), where the interface states are shown with red and the real boundary modes are shown with blue (both for left and right edges, which are degenerate). The latter are nondispersive, connecting the extrema at the top of the

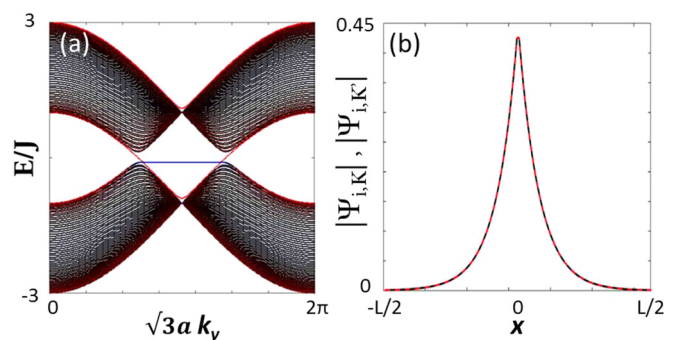


FIG. 2. (a) Ribbon dispersion [colors represent localization on the interface (red) and on the edges of the structure (blue)]. (b) Corresponding in-gap interface wave-function absolute values projection on the transverse (x) direction for K (solid black) and K' (dashed red) valleys. [Staggered potential: $\Delta_{AB}(r) = -\Delta_{AB}(l) = 0.1J$.]

valence band. On the other hand, the interface modes (red) are dispersive. They connect the valence and the conduction band in each valley, with group velocities opposite in the two valleys. Hence, this “zero-line mode,” as commonly called in the literature [12,16,38], is associated with a QVH current on the interface.

The presence of the QVH current can be understood with a topological argument based on the difference of the valley Chern numbers across the interface $N_{K,K'} = C_{K,K'}(l) - C_{K,K'}(r) = \pm 1$ (where l and r stand for the left and right domains) [16,39]. One should note that the valley Chern number is different from the Chern number of a full band. The topological charge N is used to characterize zero-line modes between two 2D Dirac vacua with inverted mass gaps [40]. In honeycomb lattices, there are two inequivalent valleys with Dirac dispersions, leading to two zero-line modes (one for each valley) at the interface.

The overlap of the wave functions of the interface states (corresponding to the wave vectors K and K') in real space in the direction perpendicular to the interface is perfect, as shown in Fig. 2(b). This implies that these states are not topologically protected against scattering on a defect between the K and K' valleys. In electronic systems, the practical argument which is put forward is that in sufficiently clean systems this kind of backscattering tends to be negligible because of the relatively large distance between the two valleys in momentum space. This argument fails in photonics, since the valleys are, on the opposite, relatively close in reciprocal space. Only some specific defect shapes, suppressing the scattering in particular directions and thus suppressing the coupling between the valleys, would keep the valley current unperturbed. On the other hand, a random disorder, such as the variation of the pillar diameter in micropillar lattices, or the variation of the hole size in photonic crystal slabs certainly induces an important scattering between the valleys. In the last section of the manuscript, we demonstrate the absence of topological protection for the valley current in the QVHE by simulating the scattering on a localized defect.

III. QUANTUM VALLEY HALL EFFECT WITH PHOTONIC SPIN-ORBIT COUPLING

We now include the light polarization degree of freedom and the so-called TE-TM spin-orbit coupling [41] (present in

any photonic system) in our model. The Hamiltonian becomes a 4×4 matrix [42] written here in the $(\Psi_A^+, \Psi_A^-, \Psi_B^+, \Psi_B^-)$ basis:

$$H_{qvh} = \begin{pmatrix} \Delta_{AB} \mathbb{I} & F_k \\ F_k^\dagger & -\Delta_{AB} \mathbb{I} \end{pmatrix}, \quad F_k = - \begin{pmatrix} f_k J & f_k^+ \delta J \\ f_k^- \delta J & f_k J \end{pmatrix}, \quad (3)$$

where δJ is the spin orbit coupling strength and f_k^\pm coefficients are defined by $f_k^\pm = \sum_{j=1}^3 \exp(-i[\mathbf{k} \cdot \mathbf{d}_{\phi_j} \mp 2\phi_j])$. The definition of valley Chern number when spin-orbit coupling is present is not strict because the SOC brings an additional contribution to the Berry curvature of each band [43] which can lead to noninteger C_K . However, if the valleys are still energetically defined (which means that they are clearly visible in the dispersion), and the two lattices on each side of the interface are perfectly inverted, the difference between valley Chern numbers $N_{K,K'}$ is a well defined integer.

A. Valley topological charges: analytical results

To demonstrate that the difference between the valley Chern numbers remains integer, we compute analytically the topological charges of the valleys in a staggered honeycomb lattice with TE-TM SOC. For this purpose, we derive an effective low-energy Hamiltonian to describe the low-energy bands (closest to the central gap) in a given valley. Indeed, a 2×2 Hamiltonian with particle-hole symmetry can be written as a superposition of Pauli matrices: $H_{\text{eff}} = \Omega \cdot \sigma$ where Ω is an effective magnetic field. Using this notation, the Berry curvature can be written as

$$\mathbf{B} = \frac{1}{2|\Omega|^3} \Omega \cdot (\partial_{q_x} \Omega \times \partial_{q_y} \Omega) \quad (4)$$

whose integral $\frac{1}{2\pi} \int \mathbf{B} \cdot \mathbf{d}\mathbf{q}$ corresponds to the winding number of the pseudospin on the Bloch sphere which is equivalent to the Chern topological invariant for 2×2 Hamiltonians.

In order to use the above picture, we need to reduce the number of states in the basis of our system. First, we linearize the 4×4 Hamiltonian defined above around the K point $(0, \frac{4\pi}{3\sqrt{3}a})$. Using the new coordinate $\mathbf{q} = (\mathbf{k} - \mathbf{K})$, we rewrite it in the basis $(\Psi_A^+, \Psi_B^-, \Psi_A^-, \Psi_B^+)$ where A/B and \pm are the sublattice and spin indices, respectively,

$$H_{qvh,K} = \begin{pmatrix} \Delta_{AB} & -\frac{3a\delta J}{2}(q_y - iq_x) & 0 & \frac{3aJ}{2}(q_y + iq_x) \\ -\frac{3a\delta J}{2}(q_y + iq_x) & -\Delta_{AB} & \frac{3aJ}{2}(q_y - iq_x) & 0 \\ 0 & \frac{3aJ}{2}(q_y + iq_x) & \Delta_{AB} & -3\delta J \\ \frac{3aJ}{2}(q_y - iq_x) & 0 & -3\delta J & -\Delta_{AB} \end{pmatrix} = \begin{pmatrix} H_1 & T \\ T & H_2 \end{pmatrix}. \quad (5)$$

We are interested in the two branches closest to the gap (the inner branches of the dispersion). The perturbation theory is applicable if the high-energy branches are sufficiently far away, which means $\delta J \gg \Delta_{AB}$. Using the perturbation theory, one can derive an effective 2×2 Hamiltonian: $H_{\text{eff}} = H_1 - T H_2^{-1} T$. In the following, we are interested in two different limits: when $\delta J \ll J$ and when $\delta J \sim J$.

In the first limit, one can neglect the term $\sim \delta J q$ (corresponding to neglect the trigonal warping [42]). The effective Hamiltonian can then be written as

$$H_{K,\text{eff}}^{(1)} = \begin{pmatrix} \Delta_{AB} & 0 \\ 0 & -\Delta_{AB} \end{pmatrix} + \frac{1}{\Delta_{AB}^2 + 9\delta J^2} \begin{pmatrix} \frac{9a^2 J^2 \Delta_{AB}}{4} q^2 & \frac{27a^2 J^2 \delta J}{4} (q_y + iq_x)^2 \\ \frac{27a^2 J^2 \delta J}{4} (q_y - iq_x)^2 & -\frac{9a^2 J^2 \Delta_{AB}}{4} q^2 \end{pmatrix}. \quad (6)$$

Due to the absence of the terms $\sim \delta J q$, when $\Delta_{AB} = 0$ the energies are two inverted parabola degenerate at $\mathbf{q} = 0$. A similar development around K' ($0, -\frac{4\pi}{3\sqrt{3}a}$) allows to obtain $H_{K',\text{eff}}$. Using Eq. (4), we compute the Berry curvature in this limit:

$$\mathbf{B}^{(1)} = \frac{\tau_z 144a^4 \Delta_{AB} J^4 \delta J^4 q^2}{(9a^4 \delta J^2 J^4 q^4 + \Delta_{AB}^2 (4\delta J^2 + a^2 J^2 q^2)^2)^{3/2}} \mathbf{e}_z, \quad (7)$$

where $\tau_z = \pm 1$ for K/K' valleys. The corresponding valley Chern number is

$$C_{K,K'}^{(1)} = \frac{1}{2\pi} \int \mathbf{B} d\mathbf{q} = \tau_z \text{sgn}(\Delta_{AB}) \left(1 - \frac{\tau_z \Delta_{AB}}{\sqrt{\Delta_{AB}^2 + 9\delta J^2}} \right). \quad (8)$$

The valley Chern numbers tend to $C_{K,K'}^{(1)} = \tau_z \text{sgn}(\Delta_{AB})$ if the high-energy bands are far away from the low-energy ones ($\Delta_{AB} \ll \delta J$). As a consequence, the topological invariant characterizing the domain wall between two inverted TMD is

$$N_{K,K'}^{(1)} = C_{K,K'}(l) - C_{K,K'}(r) = \pm 2 \text{sgn}(\Delta_{AB}), \quad (9)$$

which means that there are two co-propagating interface states in a given valley. One can see from Eq. (8), that if the high-energy bands are too close, the valley Chern number of a given low-energy band is not an integer. This means that the topological charge is shared between the high and low-energy bands. In this case, perturbation theory becomes inapplicable and one needs to compute the valley Chern numbers numerically.

In the second limit, where $\delta J \sim J$, the linear terms ($\delta J q$) have to be conserved and we can neglect the quadratic terms q^2 . The resulting effective 2×2 Hamiltonian around K and K' can be written in the (Ψ_A^+, Ψ_B^-) and (Ψ_A^-, Ψ_B^+) basis:

$$H_{K,\text{eff}}^{(2)} = \begin{pmatrix} \Delta_{AB} & \frac{3a\delta J}{2}(q_y - iq_x) \\ \frac{3a\delta J}{2}(q_y + iq_x) & -\Delta_{AB} \end{pmatrix}, \quad (10)$$

$$H_{K',\text{eff}}^{(2)} = \begin{pmatrix} \Delta_{AB} & -\frac{3a\delta J}{2}(q_y + iq_x) \\ -\frac{3a\delta J}{2}(q_y - iq_x) & -\Delta_{AB} \end{pmatrix}. \quad (11)$$

By looking at these two effective Hamiltonians, we can directly see that the signs of the diagonal elements are the same, whereas the windings of the effective in-plane fields are opposite, exactly as in staggered honeycomb lattices without SOC. Hence the Berry curvatures are opposite in each valley. They can be calculated as

$$\mathbf{B}^{(2)} = -\frac{\tau_z 9a^2 \Delta_{AB} \delta J^2}{(4\Delta_{AB}^2 + 9a^2 \delta J^2 q^2)^{3/2}} \mathbf{e}_z, \quad (12)$$

where $\tau_z = \pm 1$ for K/K' valleys. The corresponding valley Chern numbers are $C_{K,K'}^{(2)} = -\frac{\tau_z}{2} \text{sgn}(\Delta_{AB})$. The domain wall invariant between two inverted QVH phases is then $N_{K,K'}^{(2)} = \mp \text{sgn}(\Delta_{AB})$, which implies the presence of one interface mode in each valley. The group velocities of these modes in the two valleys are of course opposite.

This low-energy study has allowed us to determine analytically the valley topological charge in these two limits and hence to compute the number of valley-polarized interface states.

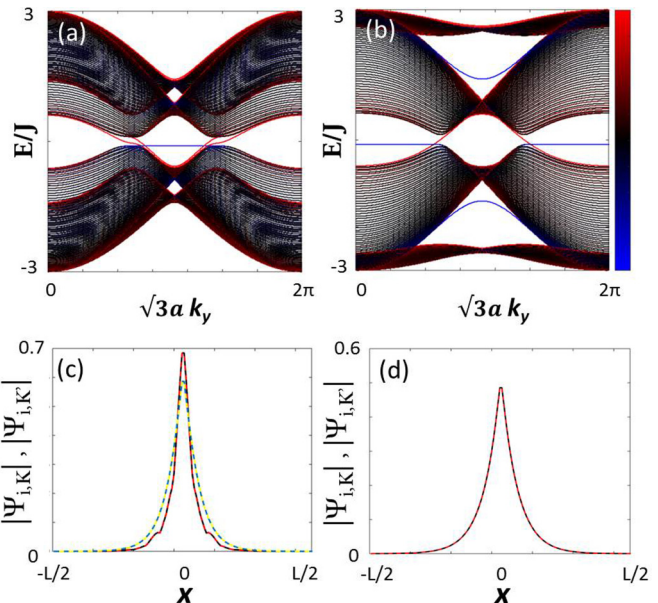


FIG. 3. (a) and (b) Ribbon dispersions with TE-TM SOC: (a) $\delta J = 0.2J$ and (b) $0.8J$. Colors represent localization on the interface (red) and on the edges of the structure (blue). (c) and (d) Corresponding absolute values of the interface wave functions in K (solid black and solid blue) and K' (dashed red and dashed yellow) valleys. [Staggered potential: $\Delta_{AB}(r) = -\Delta_{AB}(l) = 0.1J$.]

One should note that the topological charge of a given valley changes sign between the two limits. The group velocities of the interface states are inverted as well. In the appendix, we show the effective Hamiltonian derived in the general case between the two limits considered here.

B. Spectrum and discussion

In the previous section, we have derived an effective low-energy two-band Hamiltonian in order to compute analytically the valley topological charges. We have shown that it is possible to distinguish between two configurations. In the weak SOC limit, $N_{K,K'} = \pm 2 \text{sgn}(\Delta_{AB})$, whereas when $\delta J \sim J$, $N_{K,K'} = \mp \text{sgn}(\Delta_{AB})$. Here, we compute the corresponding tight-binding dispersions of the ribbon which are shown in Figs. 3(a) and 3(b), respectively. In Fig. 3(a), there are two interface states in each valley, that are visible within the band gap. The ribbon dispersion in the second limit is shown in Fig. 3(b), this time there is only one interface state in each valley, as predicted from the topological invariant. The corresponding spatial overlap of the interface wave functions in K and $-K$ valleys is shown in Figs. 3(c) and 3(d). In Fig. 3(c), we plot the two wave functions present in each valley for zero energy states (at the center of the gap). We can see a slight difference in their localization profiles, whereas they show a perfect overlap with their counterpart in the opposite valley. As in the case without SOC, the backscattering from one valley to the other is not forbidden. However, it should be noted that the presence of TE-TM SOC induces a polarization mismatch between the two valleys (not visible on these figures, showing only the absolute value of the wave function), which reduces the exact overlap of the two wave functions.

IV. PERFECT OPTICAL VALLEY FILTER

Exciton-polaritons, mixed exciton-photon quasiparticles appearing in microcavities in the strong coupling regime, are sensitive to an external magnetic field due to their excitonic part. Optical quantum anomalous Hall (QAH) effect has been predicted to occur in honeycomb lattice of polariton micropillars with TE-TM SOC under a Zeeman field [31,44]. In this section, we propose to organize an interface between this QAH phase and the QVH phase presented above, in order to obtain a perfect valley filter as sketched in Fig. 4(a), where the colored arrows represent the propagating edge states on the boundaries of the QAH phase. A similar scheme has been recently theoretically proposed for electrons in graphene with Rashba SOC [45]. However, we stress that the QAH effect has not been observed yet in graphene and that the creation of such interface in electronic systems seems quite challenging experimentally.

A. QAH phase: analytical results

The tight-binding Hamiltonian describing the photonic QAH phase is the following [31]:

$$H_{qah} = \begin{pmatrix} \Delta_z \sigma_z & F_k \\ F_k^\dagger & \Delta_z \sigma_z \end{pmatrix}, \quad (13)$$

where Δ_z is the Zeeman splitting. We propose to create a topological domain wall between QAH and QVH phases. In this subsection we derive an effective low-energy theory for

$$H_{qah,K} = \begin{pmatrix} \Delta_z & -\frac{3a\delta J}{2}(q_y - iq_x) & 0 & \frac{3aJ}{2}(q_y + iq_x) \\ -\frac{3a\delta J}{2}(q_y + iq_x) & -\Delta_z & \frac{3aJ}{2}(q_y - iq_x) & 0 \\ 0 & \frac{3aJ}{2}(q_y + iq_x) & -\Delta_z & -3\delta J \\ \frac{3aJ}{2}(q_y - iq_x) & 0 & -3\delta J & \Delta_z \end{pmatrix} = \begin{pmatrix} H_1 & T \\ T & H_2 \end{pmatrix}. \quad (14)$$

The difference between this linearized Hamiltonian and the one of QVH phase is that the signs of the diagonal elements of H_2 are inverted. In the configuration, where a two-band effective theory can be applied ($\delta J \gg \Delta_z$), we study the same limits as in the previous section: $\delta J \ll J$ and $\delta J \sim J$. In the first limit, one has

$$H_{\text{eff}}^{(1)} = \begin{pmatrix} \Delta_z & 0 \\ 0 & -\Delta_z \end{pmatrix} + \frac{1}{\Delta_z^2 + 9\delta J^2} \begin{pmatrix} -\frac{9a^2 J^2 \Delta_z}{4} q^2 & \frac{27a^2 J^2 \delta J}{4} (q_y + iq_x)^2 \\ \frac{27a^2 J^2 \delta J}{4} (q_y - iq_x)^2 & \frac{9a^2 J^2 \Delta_z}{4} q^2 \end{pmatrix}, \quad (15)$$

which implies the following Berry curvature when $\delta J \gg \Delta_z$:

$$\mathbf{B}^{(1)} = \frac{144a^4 \Delta_z J^4 \delta J^4 q^2}{(9a^4 \delta J^2 J^4 q^4 + \Delta_z^2 (a^2 J^2 q^2 - 4\delta J^2)^2)^{3/2}} \mathbf{e}_z. \quad (16)$$

A similar development at K' point giving the same result, one can deduce the two valleys Chern numbers:

$$C_{K,K'}^{(1)} = \text{sgn}(\Delta_z) \left(1 + \frac{\Delta_z}{\sqrt{\Delta_z^2 + 9\delta J^2}} \right) \approx \text{sgn}(\Delta_z). \quad (17)$$

When $\delta J \sim J$, the low-energy 2×2 Hamiltonians around K and K' can be written in (Ψ_A^+, Ψ_B^-) and (Ψ_B^+, Ψ_A^-) effective basis, respectively, as

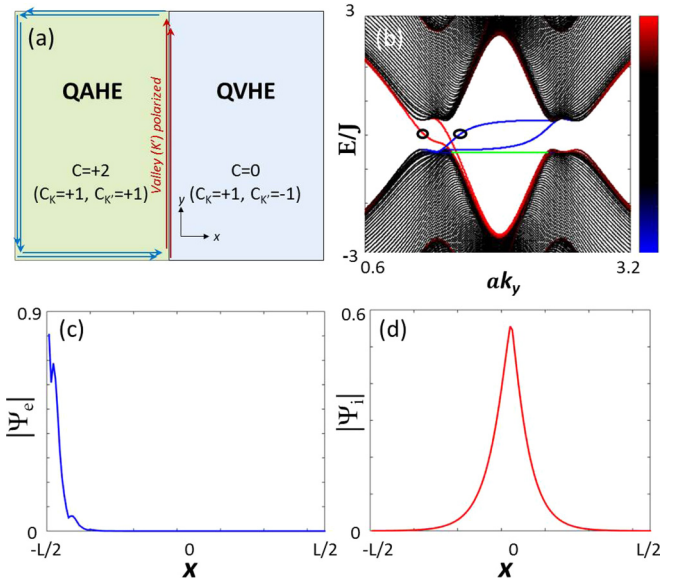


FIG. 4. (a) Scheme of the structure, (b) ribbon dispersion [colors represent localization on the interface (red) and on the left edge of the structure (blue)]. (c) and (d) Wave-function projections on the transverse (x) direction for the states highlighted by the circles in (b): (c) edge (d) interface. [Parameters: $\Delta_z(l) = \Delta_{AB}(r) = 0.1J$, $\delta J = 0.2J$, $\Delta_z(r) = \Delta_{AB}(l) = 0$.]

the QAH phase. The Hamiltonian around the K point can be written in the $(\Psi_A^+, \Psi_B^-, \Psi_A^-, \Psi_B^+)$ basis:

$$H_{K,\text{eff}}^{(2)} = \begin{pmatrix} \Delta_z & \frac{3a\delta J}{2}(q_y - iq_x) \\ \frac{3a\delta J}{2}(q_y + iq_x) & -\Delta_z \end{pmatrix}. \quad (18)$$

$$H_{K',\text{eff}}^{(2)} = \begin{pmatrix} \Delta_z & -\frac{3a\delta J}{2}(q_y - iq_x) \\ -\frac{3a\delta J}{2}(q_y + iq_x) & -\Delta_z \end{pmatrix}. \quad (19)$$

We can see that both the Zeeman field and the winding of the in-plane field have the same sign which results in equal Berry curvatures,

$$\mathbf{B}^{(2)} = -\frac{9a^2 \Delta_z \delta J^2}{(4\Delta_z^2 + 9a^2 \delta J^2 q^2)^{3/2}} \mathbf{e}_z, \quad (20)$$

leading to valley topological charges $C_{K,K'}^{(2)} = -\frac{1}{2}\text{sgn}(\Delta_z)$. These analytical results are useful to understand the behavior of the topologically protected edge states of a quantum anomalous Hall phase at the interface with a QVH phase, where the two valleys are not equivalent. Using the domain wall topological invariant $N_{K,K'}$ allows to predict the number of *topologically protected* interface states in a given valley. Of course, this topological argument is valid only when the valleys are energetically well defined.

B. Spectrum and discussion

As above, we use a tight-binding approach in order to find the edge states. The two domains are described by H_{qah} and H_{qvh} , respectively. We consider a realistic configuration for a lattice of micropillars where the TE-TM SOC is relatively weak ($\delta J < J/2$).

In the left phase, the total Chern number is equal to $C(l) = 2 \times \text{sgn}(\Delta_z)$ whereas in the right one $C(r) = 0$, as explained above. From the bulk-boundary correspondence, the interface supports two modes propagating in the same direction, given by the sign of Δ_z . When the valleys are energetically well defined, one can compute the valley Chern numbers at each side analytically (previous subsection) or numerically. In the weak δJ limit, $C_K(l) = C_{K'}(l) = \text{sgn}(\Delta_z)$ in the left domain, whereas $C_K(r) = -C_{K'}(r) = \text{sgn}(\Delta_{AB})$ in the right domain. The resulting domain wall invariants for each valley are

$$N_{K,K'} = \text{sgn}(\Delta_z) \mp \text{sgn}(\Delta_{AB}). \quad (21)$$

We stress here that even if the valley Chern numbers are not well defined integers for all range of parameters, their difference $N_{K,K'}$ defined above is always an integer. Therefore the domain wall invariant always cancels for one valley, and is nonzero for the other valley. The two one-way modes are therefore always valley polarized.

To confirm this analysis based on topological argument, we compute the dispersion of a semi-infinite ribbon as we did in the previous sections. The results are shown in Fig. 4. In panel (b), we can see that the interface states (red) are localized in one of the two valleys in momentum space. The nondispersive edge states of the QVH phase are shown in green. The one-way dispersive edge states of the QAH phase (blue) cross the gap and connect the two valleys. Contrary to the interface between two QVH phases, there is no interface state crossing the gap in the second valley. This means that the valley polarized interface states are really topologically protected against backscattering in the presence of defects. As sketched in Fig. 4(a), the topologically protected edge states are purely valley polarized due to the domain wall topological invariant N . To clarify the difference between this scheme and the interface between two QVH phases described in the previous section, we plot in Figs. 4(c) and 4(d) the *edge* and *interface* state wave function (absolute values) projections in the x direction. We can see that the blue state is clearly localized on the left edge of the structure and only the red ones are localized on the interface. This visual argument allows to understand the topological protection due to the absence of spatial overlap between the two wave functions contrary to the case presented in the previous sections [Figs. 3(c) and 3(d)].

V. NUMERICAL SIMULATIONS

In this part, we present the full numerical simulations using the Schrödinger equation that we have performed in order to confirm the different results obtained in the tight-binding approach. We describe the evolution of polaritons in the honeycomb lattice potential by solving the spinor Schrödinger equation for polaritons (in the parabolic approximation close to the bottom of the LPB),

$$i\hbar \frac{\partial \psi_{\pm}}{\partial t} = -\frac{\hbar^2}{2m} \Delta \psi_{\pm} - \frac{i\hbar}{2\tau} \psi_{\pm} \pm \Delta_z \psi_{\pm} + \beta \left(\frac{\partial}{\partial x} \mp i \frac{\partial}{\partial y} \right)^2 \psi_{\mp} + U \psi_{\pm} + \hat{P}, \quad (22)$$

where $\psi_{\pm}(\mathbf{r}, t)$, $\psi_{-}(\mathbf{r}, t)$ are the two circular components, $m = 5 \times 10^{-5} m_{el}$ is the polariton mass, $\tau = 30$ ps the lifetime, β is the TE-TM coupling constant (corresponding to a 5% difference in the longitudinal and transverse masses). Δ_z is the magnetic field [applied only in the “Z” (applied only in the QAH region) region], U is the lattice potential (radius of the pillars $r = 1.5 \mu\text{m}$, lattice parameter $a = 2.5 \mu\text{m}$), which for some simulations includes an additional defect potential (a Gaussian potential of 1 meV and $\sigma_{\text{def}} = 1 \mu\text{m}$) centered on a certain pillar at the interface, and \hat{P} is the pump operator. We have generated 2 lattice potentials: one for staggered honeycomb lattice and one for unperturbed honeycomb lattice. In the staggered lattice, the deviation of the pillar radius from the average value was chosen to be 15%. Depending on the configuration (QVH/QVH phases or QVH/QAH phases), we either excite a large spot with a well-defined superposition of wave vectors corresponding to a single valley of the TMD lattice (QVH phase), or a single pillar of the Z insulator (QAH phase), but always with the frequency within the bulk gap.

Figure 5(a) shows the dispersion of the bulk TMD analog lattice. The dispersion is obtained by solving the Schrödinger equation (22) over time, which gives the time-dependent wave function $\psi_{\pm}(\mathbf{r}, t)$, which is then Fourier-transformed to give the intensity as a function of energy and wave vector $n(\mathbf{k}, E) = |\psi(\mathbf{k}, E)|^2$, plotted in Fig. 5. In experiments, such dispersion is usually obtained under nonresonant pumping, which can be described by choosing the pump operator \hat{P} as a random uncorrelated Gaussian noise. In numerical

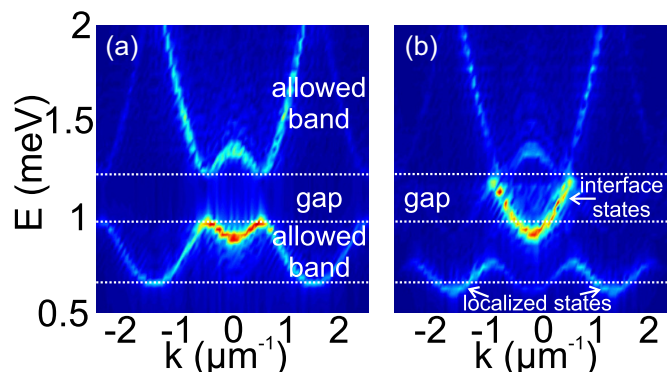


FIG. 5. Dispersion of the bulk TMD (a) and the TMD/TMD interface states in its gap (b). The boundaries of allowed and forbidden bands (the gap) are marked by dashed white lines.

experiments, one can also consider a short narrow Gaussian pulse $\hat{P} = A_0 e^{-(x-r_0)^2/\sigma^2 - (t-t_0)^2/\tau_0^2}$, where A_0 is the amplitude, r_0 is the position of the center of the pump, $\sigma = 0.7 \mu\text{m}$ is its spatial extension, and $\tau_0 = 1 \text{ ps}$ is its duration. This allows highlighting only a part of the whole dispersion (for example, only the interface states). The image in Fig. 5 is a cut of a 2D dispersion in the KMK' direction. Such representation allows to better visualize the edge of the Brillouin zone and the gap (shown by dashed white line). Panel (b) shows the dispersion of the states localized on the interface between two mutually inverted TMD analog lattices. To obtain it, the pump was centered on one of the interface pillars. The main intensity comes from the valley-polarized gap states (in the middle). However, the junction of two large pillars at the interface represents a potential trap even without taking into account the staggering inversion, and the localized states of this trap are also visible in panel (b) below the bulk band of panel (a). These states are not valley-polarized, because they are centered at the Γ point. Most interesting are the states in the central gap, which clearly exhibit opposite group velocities for the K and K' valleys. To excite these interface states, the laser spot was localized at the interface. This also suppresses the excitation of the bulk, whose dispersion therefore does not appear on panel (b).

While the TE-TM splitting was neglected for the calculation of the dispersion in Fig. 5 in order to obtain a clear image with a higher resolution, we have then included the TE-TM splitting in all numerical calculations presented below, both for QVH/QVH and QVH/QAH interfaces. All spatial images shown below are snapshots taken from the corresponding video files available in Ref. [46]. These spatial images show the total intensity of emission, given by $|\psi_+|^2 + |\psi_-|^2$, as a function of spatial coordinates x and y . The color map is renormalized for each frame, so the overall decay is not visible. Since the duration of the simulations is several hundred picoseconds, observation of the propagation over the whole structure could be experimentally possible only in the most recent highest-quality microcavities, where the polariton lifetime reaches 270 ps [47]. However, propagation around one corner or through a single defect should be well observable in the structures of previous generation with $\tau = 30 \text{ ps}$. In these simulations, the pulse duration has to be much longer than for the calculation of the dispersion: the energy width of the pulse has to be smaller than the gap. We have used a value of $\tau_0 = 36 \text{ ps}$, as in previous similar works [31]. The spatial configuration of the pump operator is different for the QVH and QAH cases. For QVH, the choice of the valley is determined by the shape of the pump, which is therefore a large Gaussian spot $\sigma = 15 \mu\text{m}$, centered on a given valley in the reciprocal space by introducing spatial modulation $\exp(i\mathbf{K}\mathbf{r})$, which in experiments is obtained by the incidence angle of the pumping laser. For QAH, only one propagation direction is available and the shape of the spot does not play any role; we therefore excite a single pillar using $\sigma = 1 \mu\text{m}$.

Figure 6(a) demonstrates the behavior of interface states at the 120° corners (meaning that the propagation direction changes by 120°) of a polygonal interface between two mutually inverted TMD analog lattices. Such angle allows to have two interfaces of the same type (A-A and A-A or B-B and B-B). As can be seen from the figure and from the associated movie (see Ref. [46], video file 1), there is no backscattering

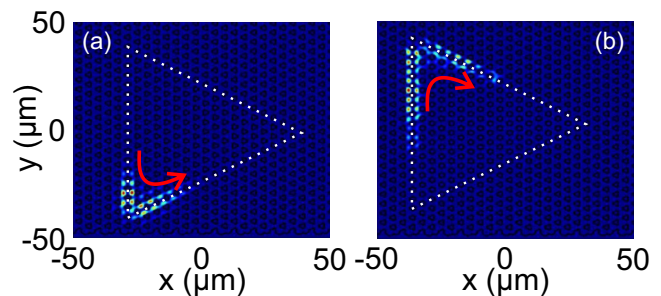


FIG. 6. Behavior at the 120° corners of polygonal interface (a) QVH/QVH and (b) QVH/QAH. Red arrows show the propagation direction.

on such interface and the wave packet, initially created at the interface states, continues its propagation without being perturbed by such corner. Qualitatively, such corner acts like a mirror (formed by the periodic lattice), which redirects the wave packet from the input interface state into the output interface state. Both propagation directions along the triangle are available by the choice of the initial valley excitation. Panel (b) shows the same configuration, but for an interface between the QVH/QAH phases. Here, no backscattering is possible for any type of corner, as we shall see below, because of the topological protection. The propagation direction is not defined by the excitation conditions (a single pillar of the interface is excited), but by the sign of the Zeeman splitting. However, a large gap is more difficult to obtain in the QAH phase [44], and therefore one can expect to have a larger excitation of the bulk in this case. As can be seen from the movie (see Ref. [46], video file 3), it is impossible to distinguish the topologically protected QVH/QAH phase from the QVH/QVH interface which does not provide any topological protection. The absence of backscattering in one particular experiment does not mean that the system is protected completely, as we shall see below.

Figure 7 shows a zoomed image of a more interesting configuration, corresponding to a 60° turn of the interface. Panel (a) shows the interface between the two QVH phases. For such angle, the interface changes type (from A-A to B-B or vice versa), which leads to several visible effects. First of all, the change of the interface type, similar to the change of dimerization order in the Su-Schrieffer-Heeger model [48],

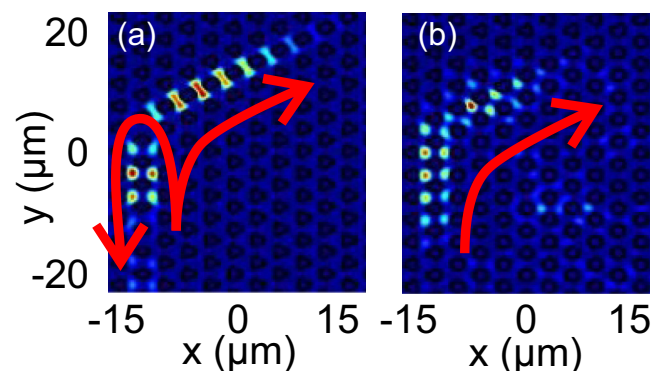


FIG. 7. Conversion of the interface states at the 60° corners of polygonal interface (a) QVH/QVH and (b) QVH/QAH. Red arrows show the propagation direction.

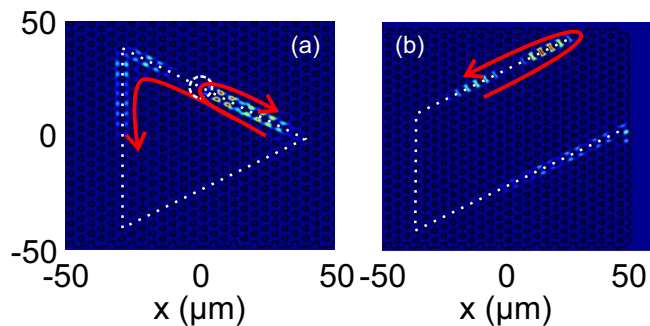


FIG. 8. Sensitivity of the QVH interface states to the perturbations: backscattering (a) on a localized defect (b) at the boundary with the “vacuum.” Red arrows show the propagation direction.

leads to the creation of a defect state (domain wall) between the two regions. This domain wall creates a strong backscattering for the wave packet on the interface states, contrary to the 120° turn, where the backscattering was completely absent. Moreover, since the interface changes type, the nature of the state changes as well: from the “antibonding” state of the first interface (made of two pillars with a larger radius and therefore a lower energy), the state changes into the “bonding” state of the second interface (where there are two smaller pillars). The two red arrows mark the propagation direction for the backscattered part and the main part of the wave packet. The propagation direction for both of them is clearly visible in the movie (see [46], video file 2).

In the QVH/QAH interface case, shown in Fig. 7(b), no backscattering is possible because of the topological protection, provided by the QAH phase, but the interface state also changes its nature at the 60° turn. However, because of the complicated mutual action of the TE-TM SOC and of the Zeeman splitting, it is more difficult to analyze from the spatial pattern of the total intensity. The study of such interface junctions in the perfect valley filter may be a subject for future works. While it is not so clear from the snapshot, the associated movie (see Ref. [46], video file 4) clearly shows the absence of backscattering at the junction.

Finally, we have designed a special numerical experiment to show that the QVH states indeed do not provide topological protection from backscattering. Figure 8 shows two distinct situations. Panel (a) demonstrates that a localized defect

(created on a single pillar on the interface) leads to the backscattering of an important fraction of the wavepacket (red arrows), while at the same experiment the corners have shown no backscattering, and one might have concluded that the states are protected (see Ref. [46], video file 1). Panel (b) (which corresponds to the calculation of Fig. 7(a) at later times, see [46], video file 2) shows that the interface states can only exist on the interface between two inverted TMD analog lattices, and they cannot propagate at the boundary between the TMD analog and the “vacuum” (absence of pillars). Such boundary leads to complete reflection of the propagating wave packet.

VI. CONCLUSION

In this work, we highlight the analogy between electronic TMD materials and a honeycomb array of photonic pillar cavities. The control of the size of the pillars allows to control the gap in the dispersion. Valley-polarized modes are predicted at the interface between two mutually inverted TMD lattices. We study these states, taking into account the TE-TM SOC, typical for cavity systems. We show that the control of the TE-TM SOC allows to control the number and group velocity of the interfaces modes. The observation of QVHE with light should be achievable in sufficiently regular structures.

In the second part, we propose a scheme to engineer a perfect valley filter using the interface between a QVH phase and a QAH phase predicted for polariton systems. In this configuration, the interface valley-polarized states are topologically protected against back-scattering and bulk diffusion. Our results are supported by analytics (the computation of topological charges), tight-binding numerical dispersions, and full numerical simulations. As in several previous works [44,49], the effective Zeeman fields can be controlled by optical pumping thanks to the spin-anisotropic interactions. This opens the perspective to realize all-optically controlled, reconfigurable valley filters. Another interesting perspective is the study of the physics of interacting bosonic quantum fluids [50] in topological systems [51–56], such as, for instance, chiral nonlinear gap states [57].

ACKNOWLEDGMENTS

We acknowledge the support of the projects: “Quantum Fluids of Light” (ANR-16-CE30-0021) and the “Investissement d’avenir” programs GANEX (ANR-11-LABX-0014) and IMOBS3 (ANR-10-LABX-16-01).

APPENDIX: EFFECTIVE 2 BY 2 HAMILTONIAN WITH TRIGONAL WARPING

Between the two limits considered in the text to compute analytically valley topological charges, it is still possible to write an effective 2×2 Hamiltonian:

$$H_{K,\text{eff}} = \begin{pmatrix} \Delta_{AB} & \frac{3a\delta J}{2}(q_y - iq_x) \\ \frac{3a\delta J}{2}(q_y + iq_x) & -\Delta_{AB} \end{pmatrix} + \frac{1}{\Delta_{AB}^2 + 9\delta J^2} \begin{pmatrix} \frac{9a^2 J^2 \Delta_{AB}}{4} q^2 & \frac{27a^2 J^2 \delta J}{4} (q_y + iq_x)^2 \\ \frac{27a^2 J^2 \delta J}{4} (q_y - iq_x)^2 & -\frac{9a^2 J^2 \Delta_{AB}}{4} q^2 \end{pmatrix}. \quad (\text{A1})$$

This effective Hamiltonian allows to compute the energy dispersion taking into account the trigonal warping. Moreover, one can also compute the Berry curvature of the low-energy bands, which can be written as follows in polar coordinates (q, ϕ) :

$$\mathbf{B} = -\frac{\tau_z 18a^2 \Delta_{AB} \delta J^4 (4\delta J^4 - a^2 J^2 (\delta J^2 + 4J^2) q^2 + a^3 J^4 q^3 \sin(3\phi))}{(\Delta_{AB}^2 (4\delta J^2 + a^2 J^2 q^2)^2 + 9a^2 \delta J^2 q^2 (4\delta J^4 + a^2 J^4 q^2) + 36a^3 \delta J^4 J^2 q^3 \sin(3\phi))^{3/2}}. \quad (\text{A2})$$

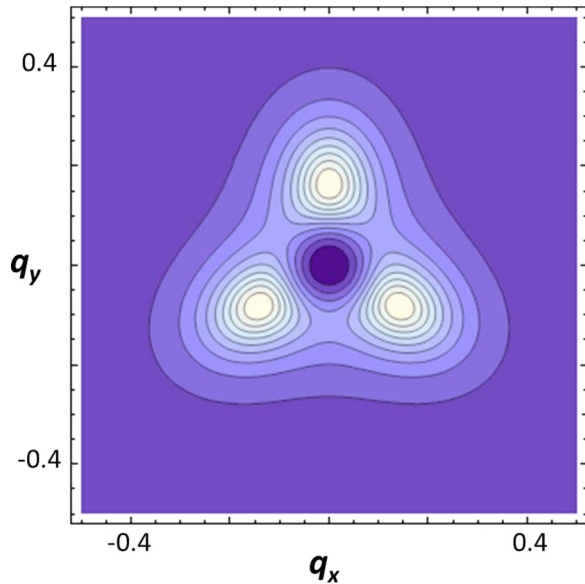


FIG. 9. Berry curvature around K point with trigonal warping contribution [Eq. (A2)]. [Parameters: $\Delta_{AB}(r) = 0.1J$, $\delta J = 0.2J$.]

The form of the resulting Berry curvature describes well the additional bands extrema contributions (see Fig. 9). This quantity is not integrable analytically but converge numerically to 2π when $\delta J \gg \Delta_{AB}$. Each additional Dirac points, located at $\vec{l}_1 = (0, \frac{2\delta J^2}{aJ^2})$, $\vec{l}_2 = (\frac{\sqrt{3}\delta J^2}{aJ^2}, -\frac{\delta J^2}{aJ^2})$, $\vec{l}_3 = (-\frac{\delta J^2}{aJ^2}, -\frac{\sqrt{3}\delta J^2}{aJ^2})$, carrying π , whereas the central one carries $-\pi$. However, this low-energy effective theory does not carry information about the second valley. When δJ increases, the additional Dirac points of the K and K' carrying opposite topological charges move in opposite directions on the same line KK' and cancel each other for some critical parameters due to the finite size of the Brillouin zone. Then, the second limit, with $C_{K,K'}^{(2)} = -\tau_z \frac{1}{2} \text{sgn}(\Delta_{AB})$, discussed in the main text is achieved when the concept of valley is again well defined, that is, when δJ becomes sufficiently large.

[1] P. R. Wallace, *Phys. Rev.* **71**, 622 (1947).
 [2] D. Xiao, M.-C. Chang, and Q. Niu, *Rev. Mod. Phys.* **82**, 1959 (2010).
 [3] D. Xiao, W. Yao, and Q. Niu, *Phys. Rev. Lett.* **99**, 236809 (2007).
 [4] D. Xiao, G.-B. Liu, W. Feng, X. Xu, and W. Yao, *Phys. Rev. Lett.* **108**, 196802 (2012).
 [5] M. Trushin, M. O. Goerbig, and W. Belzig, *Phys. Rev. B* **94**, 041301 (2016).
 [6] H. Zeng, J. Dai, W. Yao, D. Xiao, and X. Cui, *Nat. Nanotechnology* **7**, 490 (2012).
 [7] K. F. Mak, K. He, J. Shan, and T. F. Heinz, *Nat. Nanotechnology* **7**, 494 (2012).
 [8] W. Yao, D. Xiao, and Q. Niu, *Phys. Rev. B* **77**, 235406 (2008).
 [9] T. Cao, G. Wang, W. Han, H. Ye, C. Zhu, J. Shi, Q. Niu, P. Tan, E. Wang, B. Liu *et al.*, *Nat. Commun.* **3**, 887 (2012).
 [10] K. F. Mak, K. L. McGill, J. Park, and P. L. McEuen, *Science* **344**, 1489 (2014).
 [11] C. L. Kane and E. J. Mele, *Phys. Rev. Lett.* **95**, 146802 (2005).
 [12] G. W. Semenoff, V. Semenoff, and F. Zhou, *Phys. Rev. Lett.* **101**, 087204 (2008).
 [13] W. Yao, S. A. Yang, and Q. Niu, *Phys. Rev. Lett.* **102**, 096801 (2009).
 [14] E. McCann, *Phys. Rev. B* **74**, 161403 (2006).
 [15] E. V. Castro, K. S. Novoselov, S. V. Morozov, N. M. R. Peres, J. M. B. Lopes dos Santos, J. Nilsson, F. Guinea, A. K. Geim, and A. H. C. Neto, *Phys. Rev. Lett.* **99**, 216802 (2007).
 [16] I. Martin, Y. M. Blanter, and A. F. Morpurgo, *Phys. Rev. Lett.* **100**, 036804 (2008).
 [17] J. Li, I. Martin, M. Büttiker, and A. F. Morpurgo, *Nat. Phys.* **7**, 38 (2011).
 [18] F. Zhang, A. H. MacDonald, and E. J. Mele, *Proc. Natl. Acad. Sci. U.S.A.* **110**, 10546 (2013).
 [19] E. V. Castro, N. M. R. Peres, J. M. B. Lopes dos Santos, A. H. C. Neto, and F. Guinea, *Phys. Rev. Lett.* **100**, 026802 (2008).
 [20] L. Ju, Z. Shi, N. Nair, Y. Lv, C. Jin, J. Velasco Jr, C. Ojeda-Aristizabal, H. A. Bechtel, M. C. Martin, A. Zettl *et al.*, *Nature (London)* **520**, 650 (2015).
 [21] A. Vaezi, Y. Liang, D. H. Ngai, L. Yang, and E.-A. Kim, *Phys. Rev. X* **3**, 021018 (2013).
 [22] E. C. Marino, L. O. Nascimento, V. S. Alves, and C. M. Smith, *Phys. Rev. X* **5**, 011040 (2015).
 [23] Y. Ren, Z. Qiao, and Q. Niu, *Rep. Prog. Phys.* **79**, 066501 (2016).
 [24] H. Pan, Z. Li, C.-C. Liu, G. Zhu, Z. Qiao, and Y. Yao, *Phys. Rev. Lett.* **112**, 106802 (2014).
 [25] T. Ozawa and I. Carusotto, *Phys. Rev. Lett.* **112**, 133902 (2014).
 [26] S. Barik, H. Miyake, W. DeGottardi, E. Waks, and M. Hafezi, *New J. Phys.* **18**, 113013 (2016).
 [27] T. Ma, A. B. Khanikaev, S. H. Mousavi, and G. Shvets, *Phys. Rev. Lett.* **114**, 127401 (2015).
 [28] T. Ma and G. Shvets, *New J. Phys.* **18**, 025012 (2016).
 [29] X.-D. Chen and J.-W. Dong, *arXiv:1602.03352*.
 [30] T. Jacqumin, I. Carusotto, I. Sagnes, M. Abbarchi, D. D. Solnyshkov, G. Malpuech, E. Galopin, A. Lemaître, J. Bloch, and A. Amo, *Phys. Rev. Lett.* **112**, 116402 (2014).
 [31] A. V. Nalitov, D. D. Solnyshkov, and G. Malpuech, *Phys. Rev. Lett.* **114**, 116401 (2015).
 [32] T. Karzig, C.-E. Bardyn, N. H. Lindner, and G. Refael, *Phys. Rev. X* **5**, 031001 (2015).
 [33] C.-E. Bardyn, T. Karzig, G. Refael, and T. C. H. Liew, *Phys. Rev. B* **91**, 161413 (2015).
 [34] D. R. Gulevich, D. Yudin, I. V. Iorsh, and I. A. Shelykh, *Phys. Rev. B* **94**, 115437 (2016).
 [35] A. Kavokin, J. J. Baumberg, G. Malpuech, and F. P. Laussy, *Microcavities* (OUP, Oxford, 2011), Vol. 16.
 [36] I. Shelykh, A. Kavokin, Y. G. Rubo, T. Liew, and G. Malpuech, *Semicond. Sci. Technol.* **25**, 013001 (2009).

- [37] M. Milićević, T. Ozawa, P. Andreakou, I. Carusotto, T. Jacqmin, E. Galopin, A. Lemaître, L. Le Gratiet, I. Sagnes, J. Bloch *et al.*, *2D Materials* **2**, 034012 (2015).
- [38] Y.-T. Zhang, Z. Qiao, and Q.-F. Sun, *Phys. Rev. B* **87**, 235405 (2013).
- [39] J. Li, A. F. Morpurgo, M. Büttiker, and I. Martin, *Phys. Rev. B* **82**, 245404 (2010).
- [40] G. E. Volovik, *The Universe in a Helium Droplet*, International Series of Monographs on Physics Vol. 117 (Oxford University Press on Demand, Oxford, 2003).
- [41] D. Solnyshkov and G. Malpuech, *C. R. Phys.* **17**, 920 (2016).
- [42] A. V. Nalitov, G. Malpuech, H. Tercas, and D. D. Solnyshkov, *Phys. Rev. Lett.* **114**, 026803 (2015).
- [43] O. Bleu, G. Malpuech, and D. Solnyshkov, [arXiv:1612.02998](https://arxiv.org/abs/1612.02998).
- [44] O. Bleu, D. D. Solnyshkov, and G. Malpuech, *Phys. Rev. B* **95**, 115415 (2017).
- [45] H. Pan, X. Li, F. Zhang, and S. A. Yang, *Phys. Rev. B* **92**, 041404 (2015).
- [46] See Supplemental Material at <http://link.aps.org/supplemental/10.1103/PhysRevB.95.235431> for more details on the calculations.
- [47] Y. Sun, P. Wen, Y. Yoon, G. Liu, M. Steger, L. N. Pfeiffer, K. West, D. W. Snoke, and K. A. Nelson, *Phys. Rev. Lett.* **118**, 016602 (2017).
- [48] W. P. Su, J. R. Schrieffer, and A. J. Heeger, *Phys. Rev. B* **22**, 2099 (1980).
- [49] O. Bleu, D. D. Solnyshkov, and G. Malpuech, *Phys. Rev. B* **93**, 085438 (2016).
- [50] I. Carusotto and C. Ciuti, *Rev. Mod. Phys.* **85**, 299 (2013).
- [51] Y. Lumer, Y. Plotnik, M. C. Rechtsman, and M. Segev, *Phys. Rev. Lett.* **111**, 243905 (2013).
- [52] G. Engelhardt and T. Brandes, *Phys. Rev. A* **91**, 053621 (2015).
- [53] S. Furukawa and M. Ueda, *New J. Phys.* **17**, 115014 (2015).
- [54] Z.-F. Xu, L. You, A. Hemmerich, and W. V. Liu, *Phys. Rev. Lett.* **117**, 085301 (2016).
- [55] M. Di Liberto, A. Hemmerich, and C. Morais Smith, *Phys. Rev. Lett.* **117**, 163001 (2016).
- [56] D. D. Solnyshkov, A. V. Nalitov, and G. Malpuech, *Phys. Rev. Lett.* **116**, 046402 (2016).
- [57] D. D. Solnyshkov, O. Bleu, B. Teklu, and G. Malpuech, *Phys. Rev. Lett.* **118**, 023901 (2017).